An Optical Range Sensor for Mobile Robot Guidance

Nicholas Pears and Penelope Probert
Department of Engineering Science, University of Oxford, England
Email:{nick,pjp}@robots.oxford.ac.uk

Abstract

We describe the development of a large field of view laser scanning sensor, based on the lateral-effect photodiode, for short range mobile robot manoeuvres such as obstacle avoidance and docking. Synchronous detection is used to approach the theoretical limit of sensor performance. Results suggest that we are only 82% above this limit, allowing us to extend the use of lateral effect photodiodes over longer ranges than have been used traditionally, whilst maintaining class II eye safety in the sensor. Finally, we use the sensor characterisation developed in the paper to provide data for discontinuity detection algorithm based on the extended Kalman filter.

1 Introduction

This paper decribes an optical means of acquiring range data for short range mobile robot manouvres. Our sensor is active, both in the sense that it uses structured light, and in the sense that it can rotate its whole body in a horizontal plane and dynamically modify its angular scan pattern within a 40 degree range. For image position measurement, we have chosen the lateral-effect photodiode (LEP) for simplicity, low cost, and close range accuracy. A consequence of using the LEP is the importance of careful low-noise circuit design. To obtain performance near to the theoretical limit we have employed a synchronous detection method. Furthermore, in order to provide simultaneously a wide field of view and a large depth of field, a synchronised scanning triangulation geometry has been employed.

In the next section we describe the sensor: the geometrical configuration and the devices and circuits. Section 3 examines the accuracy achieved, comparing it to the theoretical performance both in magnitude and in distribution. These results allow us to insert parameters into a discontinuity detection algorithm which is based on the extended Kalman filter and described in section 4.

2 Sensor design

2.1 Image sensor and optical source

For the image position sensor, we have chosen the LEP. The LEP is often cheaper and simpler to use than a CCD and can offer a greatly improved image position resolution at shorter ranges. The range at which a CCD system begins to outperform an LEP system depends on many optical, geometric, and electrical parameters. Our system requires ranges over 1m before a 1024 pixel CCD (one-pixel resolution) becomes more accurate than a simple LEP.

The optical source is a 670nm laser diode which is modulated at 10kHz and projects an average power of 0.9mW into the scene. This power complies with the class II limit (1mW) for visible lasers.

2.2 Electronic design

Careful circuit design for low noise performance is required for the efficient use of an LEP. The 10kHz modulation on the laser diode allows us to use synchronous detection in the receiver to maximise signal to noise ratio and eliminate dc offsets.

The key elements of the electronic design are shown in fig. 1. The first stage, a transimpedance amplifier, is designed with three specifications in mind: low noise density (required for good image position resolution), very high gain (required to detect signals of a few nanoamps) and a wide bandwidth (required to include the first few harmonics of the 10kHz modulation). The requirement of a high bandwidth, which is a consequence of using square wave modulation in synchronous detection, is in direct conflict with the need for a high transimpedance ($180M\Omega$). A typical stray capacitance of 3pf in parallel with a feedback resistor of $180M\Omega$ rolls the preamplifier response off at around 300Hz, which is clearly inadequate for a 10kHz square wave signal. Amplification of the first four harmonics of the modulation requires a bandwidth greater than 70kHz. To allow this, the preamplification is divided into two stages: a transimpedance amplification,

1050-4729/93 $3.00

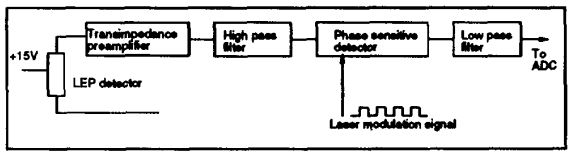

Figure 1: **The detection electronics**

implemented by a ultra low noise FET op amp, with gain 620kΩ, and a voltage amplification stage, implemented by a wide bandwidth FET op amp, with gain 150. A further factor of 1.9 is provided by later processing stages. The distribution of gain between the transimpedance and voltage amplification stages is such as to make their bandwidths equal. In this way, the total transimpedance is maximised for the chosen bandwidth (80kHz).

The function of the synchronous detection is to centre the signal content around the harmonics of the modulation, thus avoiding the effects of ambient light, dc offsets and drifts in the preamplification stages, and flicker ($\frac{1}{f}$) noise. This allows us to approach the theoretical limit of performance as defined by the white noise density over the measurement bandwidth. A high pass prefilter precedes the phase sensitive detector in order to allow for its non-ideal behaviour which is comprised of uneven mark-space ratio in the modulation, and imperfect matching of the two gains (inverting and non-inverting) in the phase sensitive detector.

The low pass filter shown in fig. 1 defines the measurement bandwidth of the system. This must be set considerably below the modulation frequency, at a level which is an appropriate compromise between signal to noise ratio and speed of response. Our filter is a fourth order filter with gain 1.9 and 3db cut off at 1kHz. Since this stage dominates the dynamic response of the system, a Bessel response was chosen to avoid any ringing at edges in the range scan.

2.3 Geometric design

A technique called synchronised scanning is often employed in multi-dimensional optical ranging in order to maintain a uniform triangulation geometry as the sensor scans over the scene. We have adopted a synchronised scheme, as suggested by Rioux [6], in which the scan direction is parallel to the detector field of view. In this geometry (see fig. 2), the scanned beam is tracked by an imaging mirror so that the angular separation between the projection axis and the optical axis of the lens remains constant.

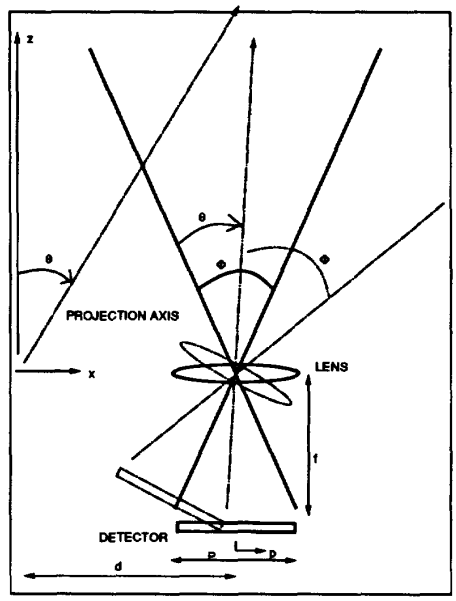

Figure 2: **Schematic synchronised scanning geometry**

We can examine easily the effect of the chosen geometry on the sensor's performance. If we assume that the range of the object is large compared with the focal length of the collecting lens, then the focal plane is at a distance f from the principal point of the lens, and simple geometrical analysis yields

$$z = \frac{fd}{p}cos^2\theta + \frac{d}{2}sin2\theta \quad (1)$$

$$x = ztan\theta \quad (2)$$

In the limit, the ratio of image resolution to range resolution is defined as the triangulation gain (G_p) and, from (1), is given by

$$\frac{\partial p}{\partial z} = G_p = \frac{fdcos^2\theta}{z^2} \quad (3)$$

Thus, for a given image resolution, ranging accuracy is proportional to source/detector separation and focal length, decreases with the inverse square of range, and decreases, moving away from the centre of a scan, by the square of the cosine. The cost of increasing accuracy with a larger baseline is a bulkier sensor and greater susceptibility to the missing parts problem. The cost of increasing accuracy by increasing focal length is a proportional reduction in the depth of field.

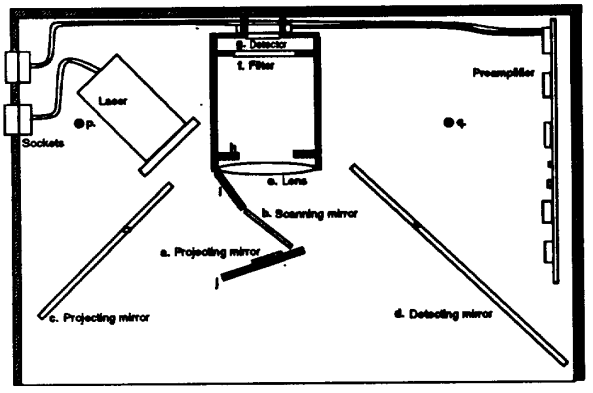

Figure 3: **The obstacle avoidance sensor**

To provide a depth of field of 0.4m to 2.5m, whilst observing these tradeoffs, we used a baseline $d = 9.5cm$, a focal length $f = 5cm$, and a detector length $P = 1cm$.

We note also that, in addition to finite image resolution, there is an effect on ranging accuracy developed by the error in measurement of the projection angle. From (1) we have

$$\frac{\partial\theta}{\partial z} = G_\theta = \frac{1}{dcos2\theta - 2ztan\theta} \tag{4}$$

A synchronised scanning head adapted from Livingstone and Rioux [3] was designed. Fig. 3 shows a plan view of the sensor, which is 21cm wide, 16cm deep, and 4.2cm high. Referring to the figure, a collimated and modulated laser beam is projected onto a small mirror (a), which deflects the beam onto the front face of the scanning mirror (b). The use of this small mirror prevents the laser body from blocking the sensor aperture. The scanned beam is then projected into the scene by a larger mirror (c), which can be pivoted to set the direction of the projection angle when the scanning mirror is at rest in its zero position. With this arrangement, the laser is scanned over twice the angle over which the scanning mirror deflects, and the centre of scanning is at the virtual image point p in the sensor.

Laser light, scattered by objects in the scene, is collected by the large adjustable detection mirror (d) and is deflected onto the rear of the scanning mirror. Light leaving the scanning mirror is focussed by the lens (e) and passes through an optical filter (f), matched to the laser wavelength, before forming an image of the projected spot on the lateral-effect photodiode (g). To minimise noise, the detector signals are amplified inside the camera head before being passed to the synchronous detector in the sensor interface rack.

With the geometry described above, the lens is effectively scanned around virtual image point q in the sensor on an arc with radius equal to the separation between the scanning mirror and the lens. In our design, this separation is kept as small as possible to minimise variations in triangulation baseline over the scanning range. The dimensions and positioning of the detection mirror (d) are critical and ensure that the full sensor aperture (the full surface of the scanning mirror) is accessible over all combinations of scan angle and target range.

The sensor is designed with as large an aperture as possible that is consistent with our scanning requirements because of the LEP's dependence on a good signal to noise ratio. Most of the aperture derives from the depth of the scanning mirror (4cm) rather than its width (2.2cm) in order to limit rotational inertia. Direct optical paths, in which laser light is focussed directly from the scene onto the LEP, have been prevented with the use of a 'cats-eye' aperture stop (h) behind the lens and shielding plates (i) and (j).

The final specifications of the sensor are: field of view (scan range) 40 degrees, depth of field (z range) 0.4m to 2.5m, samples per horizontal scan 256, scan frequency 10Hz, sample frequency 2.56kHz, projected laser power 0.9mW at 670nm (class II), detector bandwidth 1kHz (set by fourth order Bessel filter).

3 Sensor performance

Information about noise performance is needed to apply meaningful algorithms to the raw sensor scans and assess the success of our design. Here we quantify the main source of error which is due to noise currents in the image sensor and preamplifier. The full set of results and a more detailed discussion can be found elsewhere [5].

Image resolution for an LEP is given by

$$\Delta p = \frac{P}{2\frac{I_s}{I_n}} \tag{5}$$

where P is detector length and $\frac{I_s}{I_n}$ is signal current to noise current ratio. Since image position measurements are normalised to lie in the region $\{-1 \leq p \leq 1\}$, then

$$\Delta p_{norm} = \frac{I_n}{I_s} \tag{6}$$

where I_n is the total noise current over the measurement bandwidth. To quantify the uncertainty in p_{norm} we need to make an estimate of I_n (I_s is available for any reading by measurement). We can do this through determining the dependence of current on range. If

we assume that the projected spot is small enough and distant enough to be treated as a point source and that ideal, lambertian scattering occurs in the scene, then the total signal current I_s at range z can be approximated by

$$I_s = \frac{S}{z^2} \tag{7}$$

where the signal current constant, S, depends on the sensor and the environment [4]. The parameter, S, can be measured directly from a logarithmic plot of signal current against target range. For our sensor and target we find that:

$$S = 2.59 \times 10^{-8} Am^2 \tag{8}$$

Finally, substituting for I_s from equation 7 in equation 6, a logarithmic plot of image resolution against range gives the constant $\frac{I_n}{S}$ and thus the noise current I_n:

$$I_n = 36.5pA \tag{9}$$

In these tests, the measurement bandwidth was set by a fourth order low pass Bessel filter with cut off at 1kHz. Thus the approximate current noise density, assuming an ideal filter response, is

$$i_n = 1.15pAHz^{-\frac{1}{2}} \tag{10}$$

The result (9) is used to determine the standard deviation of each sensor reading in the application of the algorithm described in section 4.

An analysis of the expected noise, which has major contributions from the detector and the preamplifier [5] shows that we would expect a total current noise density (I_n) for the detector-preamplifier combination of $0.632pAHz^{-\frac{1}{2}}$. The noise density calculated from measurements ($1.15pAHz^{-\frac{1}{2}}$) is only 82% above this value, showing that the use of synchronous detection has allowed us to get close to the theoretical performance limit of the sensor. This result validates the sensor design and also gives us confidence in applying the theoretical dependence of standard deviation on signal current. In addition it suggests a Gaussian distribution of image position, since the white noise sources from which the theoretical figure was developed (thermal and shot noise) both have this distribution. This is confirmed from the experimental results described in the next section.

3.1 Measured ranging performance

In fig. 4, the crosses show the frequency with which a measurement fell within a particular range interval for a batch of 1000 measurements. The solid line shows the

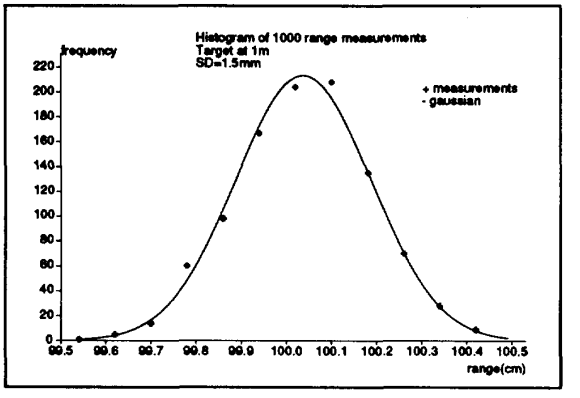

Figure 4: The distribution of range measurements at 1m

equivalent Gaussian, generated using mean and standard deviation of the batch. It is evident that, in any data processing, the assumption of a Gaussian form is reasonable. Standard deviations for a number of target ranges, and their values as a percentage of the target range, are shown in table 1.

Table 1.**Ranging accuracy**

range(m)	SD (cm)	% accuracy
0.75	0.05	0.067
1.0	0.148	0.148
1.25	0.463	0.37
1.5	0.798	0.532
1.75	1.568	1.1
2.0	2.547	1.27
2.25	3.713	1.65
2.5	7.662	3.06

3.2 Predicted ranging performance

Range resolution against range can now be plotted for the measured noise density ($1.15\ pAHz^{-\frac{1}{2}}$) and the theoretical noise density ($0.632\ pAHz^{-\frac{1}{2}}$) using

$$\Delta z = \frac{PI_n}{2fdS} z^4 \tag{11}$$

which is obtained by combining equations (5)-(7) and (3). These two plots, and the points at which ranging accuracy was measured (from table 1), are shown in fig. 5.

The data presented was collected with the mirror stationary. In scanning, there are additional ranging

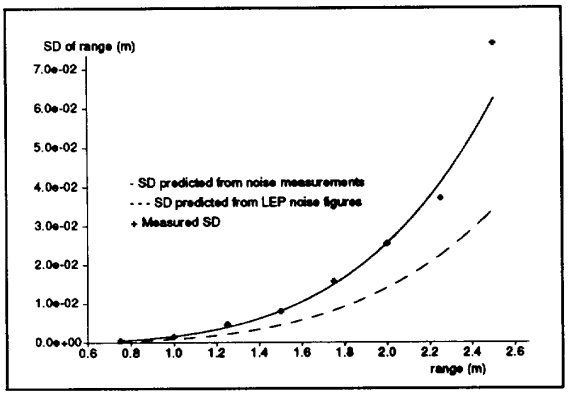

Figure 5: **Plot of predicted and actual SD of range against range**

errors due to inaccuracies in the positioning of the scanning mirror. The repeatability of the scanner suggests that these will be small compared to those due to image position resolution. Also, accuracy will be poorer at the edges of the scan than at the centre since, from (4), triangulation gain drops with $cos^2\theta$ and, to compound this, signal strength will be reduced because of the apparent reduction in aperture with $cos\theta$. The total effect is to reduce ranging accuracy at the edges of a scan to around 83% of its value at the centre.

Finally, we present raw sensor scans to illustrate the high performance in detecting edges and curves. The first plot fig. 6, shows the response over abrupt edges. The second plot, fig. 7a, shows the scan over a cylindrical object. Both figures show the deterioration of ranging performance as range increases.

Recent results have shown that signal amplitude data may be useful for localisation of certain types of feature. Fig. 7b illustrates that, in the case of a cylindrical object, a distinct peak is found at the centre of the feature.

4 Application

The immediate application will be guiding the vehicle around the edges of objects in its path, or within a docking bay. For this, the sensor must be able to recognise and locate corners, which appear as discontinuities in the image or range data. The first question we need consider is whether to process data for discontinuities in the calibrated or the uncalibrated form. It is generally easier to handle data with a well defined probability distribution, preferably Gaussian, and it is important to be able to estimate accurately the variance of each measurement. Variation in both calibration error and triangulation gain with both range and scan angle makes it difficult to estimate the variance of each point in the range scan. In contrast, the simple dependence of variance in the image plane on signal strength and estimated noise makes its estimation more straightforward and more accurate. Therefore, we are using the uncalibrated data for discontinuity detection, and subsequently calibrating points of interest into the scene coordinates.

We require a number of features from our edge detection algorithm: First it must be fast so that the sensor is not processor bound. In addition, it should be able to incorporate the variance of a measurement as well as the measurement itself, and provide results which may be used within the sensor management and data fusion schemes of a multi sensor system, as well as for local decisions. An algorithm which fulfills these requirements uses the extended Kalman filter (EKF) for tracking edges and defines a threshold for a validation gate as the basis of discontinuity detection. The EKF algorithm we used is described in detail in [1]. It is suitable for any rotating sensor in which there are equal angle increments γ between successive readings. The algorithm is fast: the filter takes about $100\mu s$ per point on a T800 transputer and it can be run on a point by point basis; it therefore operates well within the point sampling rate of 400 μ sec of the sensor.

A difficulty in using uncalibrated data is to determine the model, since edges will no longer be straight. However it is clear from our calibration curves that the non-linearity is not severe, and we were able to use a linear model without false edge detection. The model is based on the trigonometric relationship between any successive three range readings $d_{i..i+2}$ which are collinear:

$$d_{i+2} = \frac{d_i d_{i+1}}{(2d_i \cos\gamma) - d_{i+1}} \tag{12}$$

The sensitivity to the model, and of discontinuity detection, is determined by the choice of validation gate threshold [2]. The validation gate was set so that a discontinuity was marked if the observation differed from the filter's predicted observation by more than twice the standard deviation of the innovation (the difference between the observation and its prediction).

Early results from the discontinuity detection are given in figure 8, which uses the same data shown in calibrated form in figure 6. Points of insufficient signal strength (due to missing parts at edges) were removed before processing. The dynamic threshold used to eliminate missing parts data was varied in proportion to the inverse square of range in order to reflect the behaviour of signal strength.

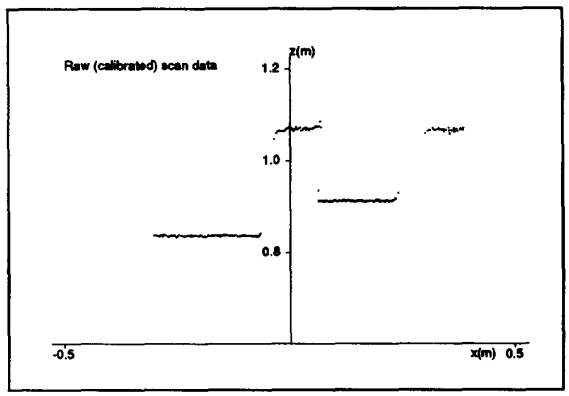

Figure 6: **Scene with boxes**

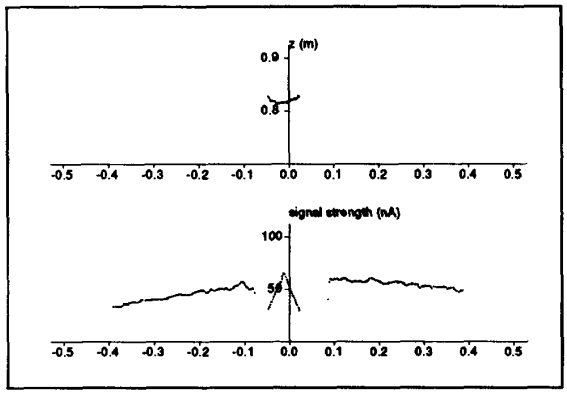

Figure 7: **Cylinder against background: range and signal strength**

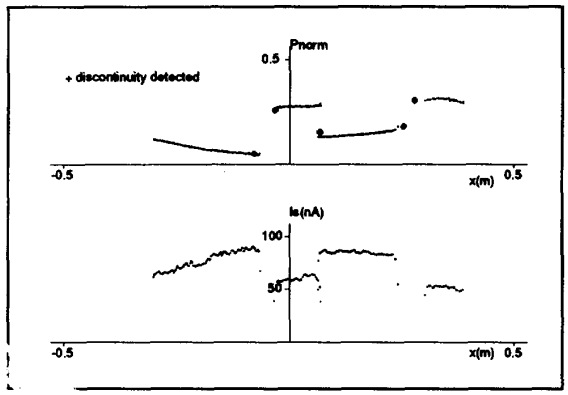

Figure 8: **Discontinuity detection in the image data**

For greater reliability, amplitude data will be used to confirm genuine discontinuities and the detected discontinuites will be tracked over consequtive scans. As well as improving the quality of discontinuity detection, this will provide information for local planning.

5 Conclusions

We have described a wide field of view range sensor for short range mobile robots manoeuvres. Measurements have shown that ranging is accurate to 0.15% at 1m, 1.3% at 2m, and 3% at 2.5m for a measurement bandwidth of 1kHz, which is suitable for real-time planning, and an average projected power of 0.9mW, which is eye-safe. These performance figures compare well with other rangefinders available at comparable cost. In addition, we have extended the application range of LEPs, which are normally used with non-eye safe lasers over much smaller depths of field.

Early results in processing show that an algorithm based on the extended Kalman filter can be used as the basis of discontinuity detection in real time, providing a basis for controlling the sensor head angle, sensor scan angle, and the robot.

References

[1] M.D. Adams. *Optical Range Data Analysis for stable target pursuit in mobile robotics.* Oxford University DPhil Thesis, 1992.

[2] Y. Bar-Shalom and T.E. Fortmann. *Tracking and Data Association.* Academic Press, 1988.

[3] F.R. Livingstone and M. Rioux. Development of a large field of view 3-d vision system. In *SPIE 665*, pages 188–194, 1986.

[4] N.E.Pears and P.J.Probert. Active triangulation rangefinder design for mobile robots. In *Proc. IEEE Workshop on Intelligent Robots and Systems*, pages 2047–2052, 1992.

[5] N.E.Pears and P.J.Probert. A lateral effect photodiode based scanning sensor for autonomous vehicle obstacle avoidance. In *1st IFAC Intl. Workshop on Intelligent Autonomous Vehicles*, 1993.

[6] M. Rioux. Laser rangefinder based on synchronised scanners. *Applied Optics*, 23(21):3837–3844, 1984.